Journal of Nanobiotechnology

RESEARCH Open Access

Specific muscle targeted delivery of miR-130a loaded lipid nanoparticles: a novel approach to inhibit lipid accumulation in skeletal muscle and obesity

Yingqian Wang[1], Zeqiang Ma[1], Lehua Jiang[2,3,4], Nataraj Bojan[1], Yiwen Sha[1], Boyu Huang[1], Lianxi Ming[1], Junnan Shen[1] and Weijun Pang[1,5*]

Abstract

Background Skeletal muscle lipid deposition is a key manifestation of obesity, often accompanied by decreased exercise capacity and muscle atrophy. Skeletal muscle as the largest organ in the body, makes it challenges for designing targeted drug delivery systems. Lipid nanoparticles (LNPs) are widely used as a safe and efficient delivery carrier, there is limited research on LNPs that specifically target skeletal muscle.

Results A LNP designed with five specific receptor complements on its surface, which specifically targets skeletal muscle in vivo in mice, without off-target effects on other tissues and organs. MiR-130a, a regulator of PPARG, which is a key factor in skeletal muscle lipid deposition, was encapsulated with LNP (LNP@miR-130a). In high-fat diet (HFD) mice, LNP@miR-130a effectively reduced skeletal muscle lipid deposition, increased exercise activity and enhanced muscle mass. Interestingly, the myokines in skeletal muscle have also changed which may leading to reduce the adipose tissue weight and liver lipid deposition in HFD mice.

Conclusions These results indicated LNP@miR-130a is a promising inhibitor of skeletal muscle lipid deposition and may help alleviate obesity. This study provides new insights for obesity treatment and lays foundation for the development of targeted skeletal muscle therapeutics.

Yingqian Wang, Zeqiang Ma and Lehua Jiang are co-first authors.

*Correspondence:
Weijun Pang
pwj1226@nwafu.edu.cn

Full list of author information is available at the end of the article

Graphical Abstract

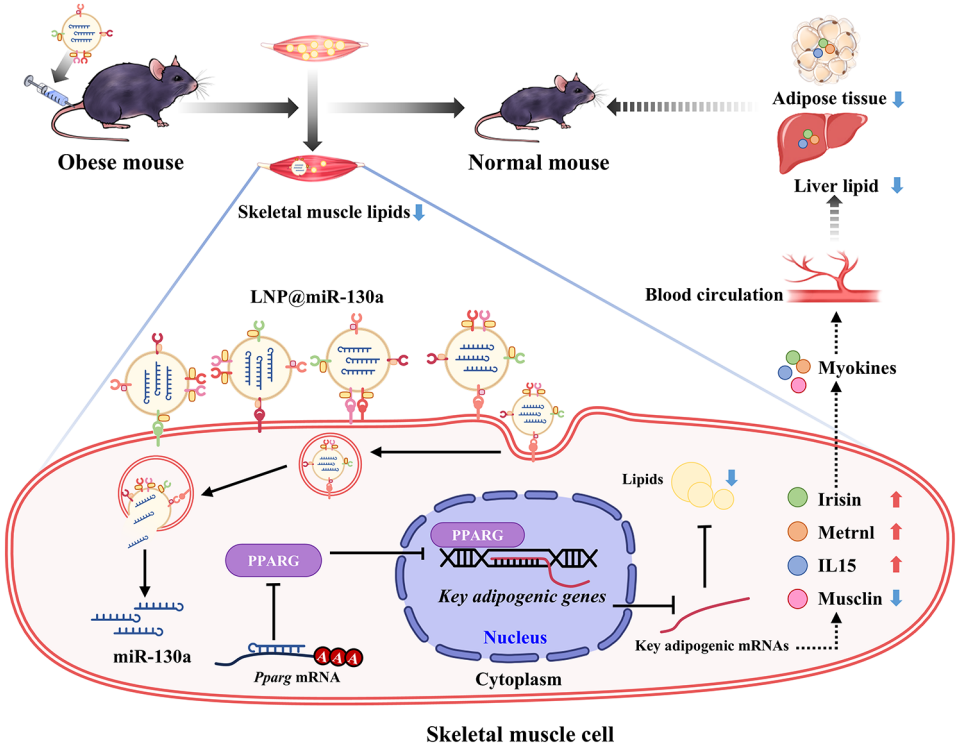

Keywords Lipid nanoparticle, LNP@miR-130a, PPARG, Skeletal muscle lipid deposition, Obesity

Introduction

Lipid nanoparticle (LNP) is an excellent carrier system composed of highly biocompatible lipids that can effectively protect nucleic acid drugs from degradation and achieve targeted delivery [1]. LNP is the most advanced nucleic acid therapy drug delivery system in clinical practice, and Onpattro was approved by the United States and the European Union in 2018 for the treatment of amyloidosis [2]. LNP has gained widespread attention as a key component of COVID-19 mRNA vaccine [3], and many liposome-based drugs have been applied in medical practice [4]. Notably, nanoparticles derived from ginger exhibit characteristics similar to mammalian extracellular vesicles, including size distribution, surface charge, morphology, density, and certain components [5], and they are easy to extract. These plant-derived extracellular vesicle-like nanoparticles (PELN), possess phospholipid bilayers can protect nucleic acids and proteins from degradation [6] suggesting that ginger derived nanoparticle as a safe and efficient phospholipid source for artificial LNP. The design of targeted carriers typically involves loading complement onto the surface of the carrier, enabling interactions with recognition elements on the cell surface, for tissue localization and selective uptake [7]. Due to the inherent properties of LNP, they are predominantly targeted to the liver, which limits their clinical applications to liver diseases and vaccines [8]. In liver-targeted research, LNP has been used to treat non-alcoholic fatty liver disease [9], liver fibrosis [10, 11]. The challenge in designing non-liver targeted LNP stems from their tendency to accumulate in the liver after intravenous administration, prompting many studies focus on enhancing the of LNP targeting to non-liver tissues [8]. Currently, there is limited research on targeting LNP to muscle tissue, and a specific lack of LNP designed for skeletal muscle diseases. Designing targeted carriers for skeletal muscle is significant challenges due to its large size and uneven drug distribution caused by intramuscular injection [12]. Based on above reasons, designing LNP for muscle tissue can help expand the targeted research of LNP and also contribute to the treatment of muscle-related diseases. Developing LNP specifically for muscle tissue could enhance targeted drug delivery and contribute to the treatment of muscle-related diseases.

Skeletal muscle lipid deposition refers to an increase lipid content like triglyceride (TG) in skeletal muscle [13], which is often a key manifestation of obesity. This condition not only impacts the function and metabolism of

skeletal muscle, but is also closely related to pathological processes such as non-alcoholic fatty liver disease [13, 14] and insulin resistance [15, 16]. Skeletal muscle is the largest metabolic organ in the body and responsible for approximately 75% of systemic glucose metabolism [17]. Altering energy metabolism in skeletal muscle can significantly aid in maintaining energy homeostasis throughout the body and serve as a regulatory method for anti-obesity [16]. In recent years, researchers' interests in obesity treatment have been increasing, and the therapeutic targets and strategies on skeletal muscles still need to be studied. In an ideal state, treatment strategies should balance therapeutic efficacy with the reduction of systemic side effects. Small non-coding RNAs have been shown to have strong therapeutic potential for obesity and metabolic syndrome [18–20]. Therefore, identifying small RNAs that inhibit lipid deposition in skeletal muscle is expected to become a promising treatment approach. MiR-130a is a crucial microRNA that plays a role in regulating lipid metabolism. It modulates the expression level of PPARG (Peroxisome Proliferator Activated Receptor Gamma) by targeting its 3'UTR, thereby affecting lipid metabolism and insulin sensitivity [21, 22]. In adipose tissue of obese individuals, miR-130a expression is reduced [18], indicating its potential as a therapeutic agent for obesity. PPARG is involved in regulating adipocyte differentiation, lipid metabolism, and the expression of inflammatory factors [23]. A study conducted transcriptome sequencing of cultured muscle cells from human lateral thigh muscles revealed that PPARG was significantly upregulated in the obese group, indicating a correlation between PPARG and skeletal muscle lipid deposition in obesity [24]. However, the role of miR-130a in reducing lipid deposition in myocytes remains unclear, and it is a challenge of accurately and efficiently delivering miR-130a into skeletal muscle. Naked miRNAs exhibit low delivery efficiency, stability, and therapeutic potential [25, 26], necessitating encapsulation for effective therapeutic outcomes and reduce systemic side effects [27]. AAV viruses are commonly used for skeletal muscle specific delivery of miRNA, however, they demonstrate low systemic delivery efficiency and may induce toxicity due to off-target effects in tissues [28]. Although LNP is an excellent carrier, specific muscle-targeting LNP carried with miR-130a needs to be designed and constructed.

In this study we have designed a LNP specifically targeting skeletal muscle, which contains five skeletal muscle-specific receptor complements on its surface and is engineered to deliver miR-130a for the treatment of skeletal muscle lipid deposition. The functional study of miR-130a provides a feasible therapeutic target for addressing abnormalities in lipid deposition skeletal muscle and obesity. Furthermore, the innovative design of this muscle-targeting LNP provides an efficient and precise delivery tool for the treatment of numerous skeletal muscle diseases.

Results

Design, synthesis and characteristic of LNP@miR-130a

LNP@miR-130a synthesis is shown in Fig. 1A. Ginger-derived nanoparticles were sonicated and broken into individual phospholipids, which were co-incubated with modified anti-receptors in a rotary distillation apparatus to form phospholipid bilayers. Together with miR-130a, they were subjected to microfluidic treatment, and miR-130a was encapsulated in LNP with antibodies on the surface. After concentration in an ultrafiltration tube, they were ready for in vivo experiments. To enhance the targeting efficiency of LNP towards skeletal muscle, we screened several proteins that are highly expressed on the surface of muscle cells as targets, including LRP-3, MYF5, MYOG, MYHC-2 A and MYHC-2B. To enhance the stability of anti-receptors, we modified LRP3, MyHC-2 A and MYF5 with mannitol, MYOG with leucine, and linked MYHC-2B with biotin-azide to form an arm like structure to stabilize the protein conformation. These modifications optimize the stability of the proteins three-dimensional structures, facilitating better penetration into target cells and improving both the activity and targeting efficiency of the LNP's (Fig. 1B).

The transmission electron microscopy (TEM) results showed no significant changes in the morphology between empty LNP and LNP@miR-130a (Fig. 2A), similarly particle size analysis also indicated no significant difference in size variation between the two formulations (Fig. 2B, C). Due to the negative charge of miRNA, LNP encapsulating miR-130a exhibited a larger negative charge value (Fig. 2D), indicating a higher encapsulation efficiency. Electrophoresis further confirmed this efficiency, as the miR-130a fragment appeared smaller than 50 bp when not encapsulated, and its size significantly increased upon encapsulation (Fig. 2E). To assess the in vivo targeting efficiency of LNP@miR-130a, we performed imaging studies three days after tail vein injection in mice (Fig. 2F). The results showed that, LNP functionalized with five different anti-receptors targeted skeletal muscle compared to the negative control and not accumulate in liver, spleen, kidneys, and lungs. Since our primary goal is to inhibit lipid deposition in mouse skeletal muscle, we also need to verify whether the therapeutic effect persisted after phenotypic changes in the mice in vivo. The treatment method for mice is depicted in Fig. 2G. After six weeks of drug administration, RNA analysis revealed that miR-130a expression in skeletal muscle was over the two-fold higher than the control group, while there was no significant change observed in adipose tissue and liver (Fig. 2H), indicating a high level of skeletal muscle specific overexpression by LNP@miR-130a.

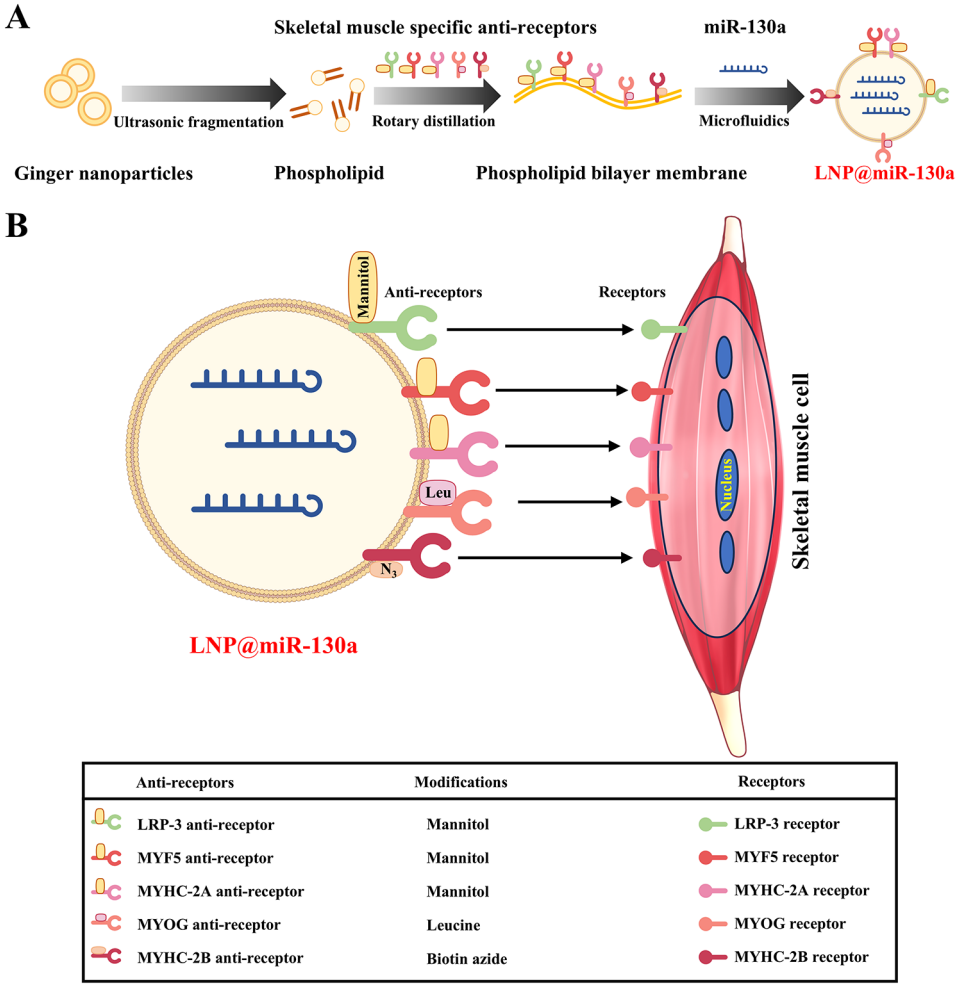

Fig. 1 Synthesis and structure of skeletal muscle specific targeting LNP@miR-130a. (**A**) Introduction to anti receptors and modifications of LNP. (**B**) The synthesis of LNP@miR-130a. Ginger exosomes were sonicated to break down into individual phospholipids, co cultured with anti-receptors to form phospholipid bilayers with antibodies, and co formed with miR-130a through a microfluidic system LNP@miR-130a

LNP@miR-130a reduces skeletal muscle lipid deposition in HFD mice

To evaluate the impact of LNP@miR-130a on lipid deposition in skeletal muscle, and mice were treated for three weeks. The control groups injected with either miR-130a alone or LNP alone, did not exhibit significant differences in weight loss compared to the normal high-fat diet (HFD) group. In contrast, the LNP@miR-130a treated group significantly decreased in body weight (Fig. 3A), with no difference in feed intake observed (Fig. 3B). In week 20, the weight difference remained below $P < 0.001$ (Fig. 3C), and there was a significant increase in the weight of *gastrocnemius muscle* (Gas) (Fig. 3D), indicating an improvement in muscle atrophy by HFD. TG analysis confirmed that LNP@miR-130a effectively reduced lipid deposition in skeletal muscle (Fig. 3E). Since obesity is often accompanied by muscle atrophy and decreased exercise ability, a series of exercise performance tests were conducted (Fig. 3F) and found that LNP@miR-130a significantly improved the physical performance of the HFD mice. Histological analysis of Gas muscle sections using H&E staining results showed a marked increase in the muscle fibers cross-sectional area after treatment (Fig. 3G, H). The Bodipy and Oil Red O staining further corroborated the TG findings, demonstrating reduced lipid content in the muscle fibers post-treatment (Fig. 3H, I, J). In addition to the gastrocnemius muscle, other skeletal muscles such as *quadriceps femoris* (Qu) and *tibialis anterior* (TA) showed increased skeletal muscle mass, enlarged muscle fiber cross-sectional area, and decreased lipid deposition in muscle fiber (Fig S1). Meanwhile, increasing the number of both Gas and Sol type I muscle fibers promote the oxidation of fat and reduce the accumulation in the muscle (Fig S2).

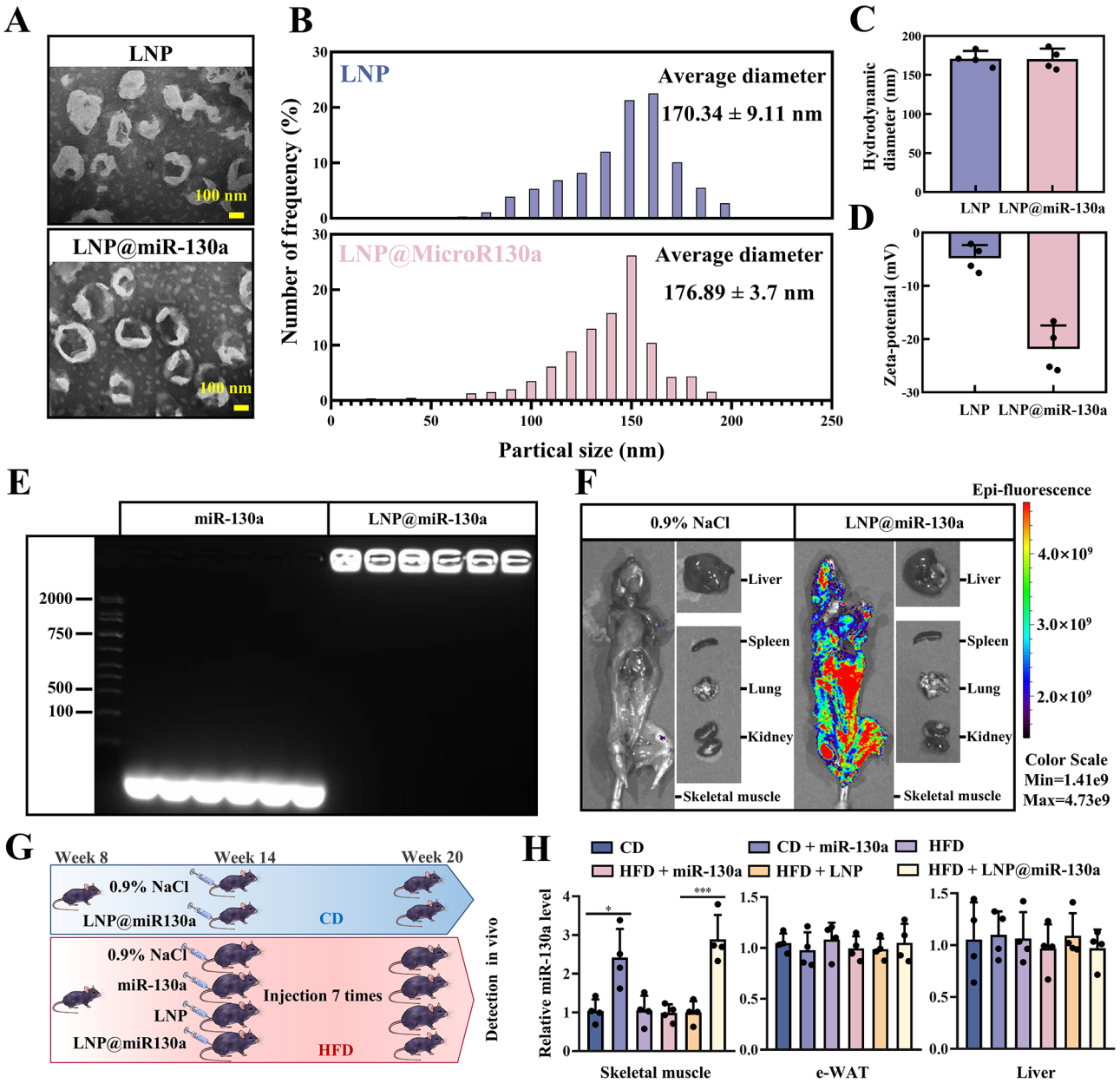

Fig. 2 Characterization and function of skeletal muscle specific targeting LNP@miR-130a. (**A**) Electron microscopy images of LNP. Scale bars = 100 nm. (**B**) Particle size distribution of LNP. (**C**) Average particle size of LNP. (**D**) Zeta potential analysis of LNP. (**E**) Electrophoretic analysis of miR-130a fragments before and after encapsulation. (**F**) Fluorescence imaging of biodistributed Cy7-labeled LNPs@miR-130a in body and ex vivo organs. (**G**) Injection process diagram for mice. (**H**) Overexpression efficiency of miR-130a in muscle, visceral e-WAT, and liver of 20 w mice. ***$P < 0.001$. For each group, $n = 4$. All data are presented as the mean ± SD

LNP@miR-130a changes the lipid metabolism pathway of skeletal muscle in HFD mice

To further investigate the effects of LNP@miR-130a on skeletal muscle of HFD mice, we collected Gas tissue from 20-weeks old mice and performed transcriptome analysis (Fig. 4A) to determine any changes in lipid metabolism-related pathways. The results showed that there was a significant overall difference between the treatment group and the control group (Fig. 4B), and the down regulated adipogenic genes included FABP4, C/EBPa, PLIN1, Adipoq, and PPARG. In contrast, mitochondrial related genes like Tfam, Mfn1, Opa1, Pgv1a upregulated (Fig. 4C). Pathway enrichment analysis was conducted for 267 down regulated genes (Fig. 4D). GO analysis (Fig. 4E) showed that the down regulated genes were primarily enriched in pathway related to cholesterol absorption, lipid absorption, adipocyte differentiation, lipid transport, lipid localization, and glucose transport.

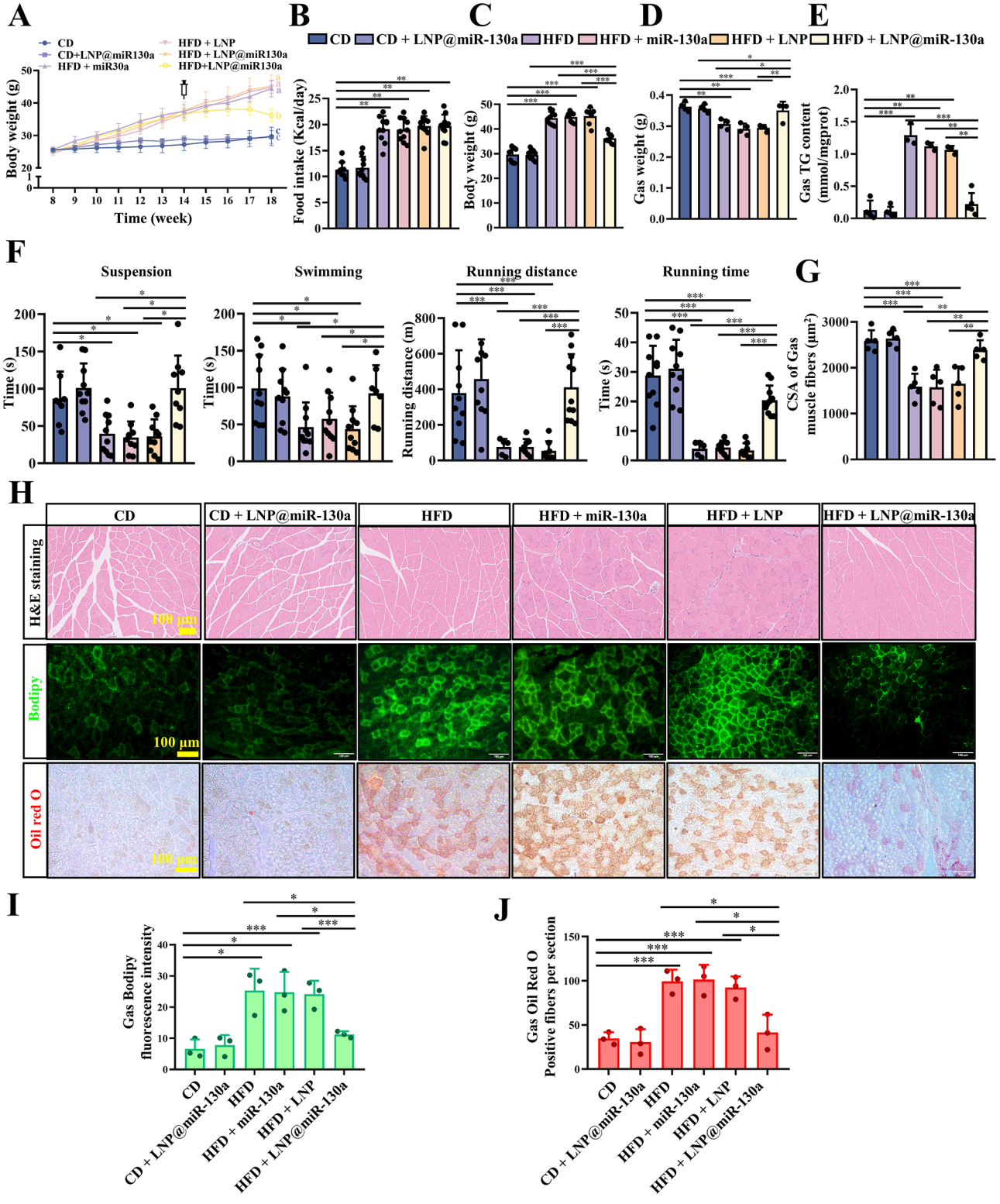

Fig. 3 LNP@miR-130a reduces lipid deposition of skeletal muscle in HFD mice. (**A**) Changes in weight of mice. Starting from 14 w, inject every three days until 17 w. $N = 10$. (**B**) Food intake of mice. $N = 10$. (**C**) Weight before slaughter of mice. $N = 10$. (**D**) Weight of Gas of mice. $N = 4$. (**E**) TG detection of gastrocnemius muscle. $N = 3 \sim 5$. (**F**) Suspension test, swimming test, treadmill test including running distance and running time. $N = 10$. (**G**) Cross sectional area statistics of gastrocnemius muscle. $N = 5$. (**H**) H&E staining, Bodipy staining and Oil Red O staining of mice Gas. Scale bars = 100 μm. (**I**, **J**) Statistics of H. $N = 3$. $^{*}P < 0.05$, $^{**}P < 0.01$, $^{***}P < 0.001$. All data are presented as the mean ± SD

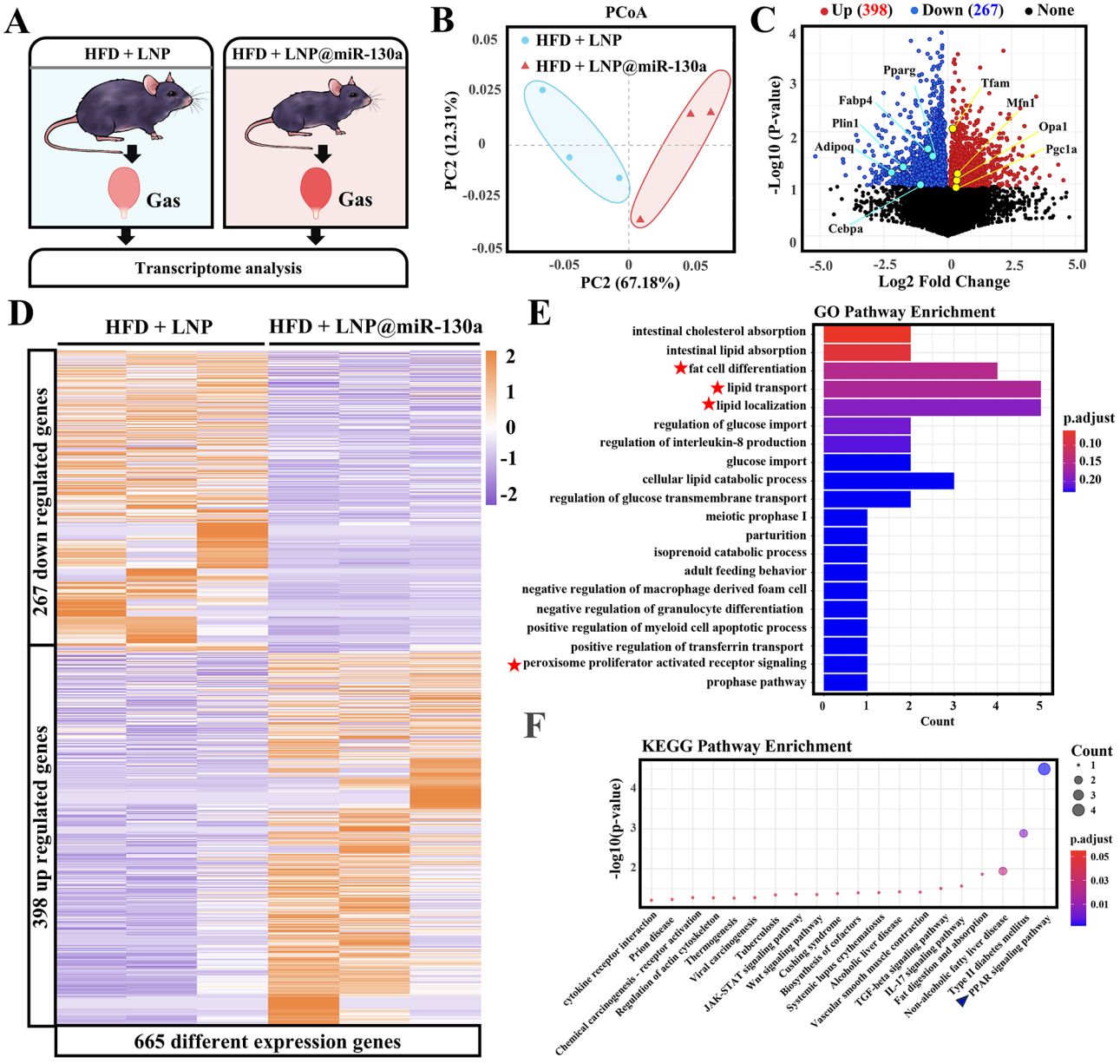

Fig. 4 LNP@miR-130a affects the lipid metabolism pathway in HFD mice. (**A**) Mouse transcriptome flowchart. (**B**) Principal component analysis. (**C**) Volcano diagram. (**D**) Heatmap of all differentially expressed genes. (**E**) GO analysis of down regulated genes. (**F**) KEGG analysis of down regulated genes. For each group, $n = 3$

KEGG analysis (Fig. 4F) revealed that these down regulated genes were mainly associated with the PPAR signal pathway, and linked to type 2 diabetes and non-alcoholic fatty liver.

LNP@miR-130a decreases lipid by interacting with PPARG in skeletal muscle

To identify the target gene of miR-130a, we analyzed the transcriptome data. The sequencing results showed that the downregulated genes were enriched in the PPAR signaling pathway, and PPARG identified as one of the target genes of miR-130a. Further, we compared the target genes detected from the sequencing data with the predicted targets of miR-130a from miRbase (https://www.mirbase.org), and found that, PPARG was the most significantly downregulated gene among the top 20 and was closely associated with adipogenesis (Fig. 5A). To confirm whether miR-130a directly binds to PPARG, we designed a dual fluorescein reporter vector (Fig. 5B) and conducted dual fluorescein reporter assays in 293T cells and C2C12 cells, respectively (Fig. 5C). The results demonstrated that the wild-type PPARG vector exhibited lower fluorescence activity with miR-130a in both cell lines, indicating that miR-130a directly binds to the 3'UTR of PPARG. Fig

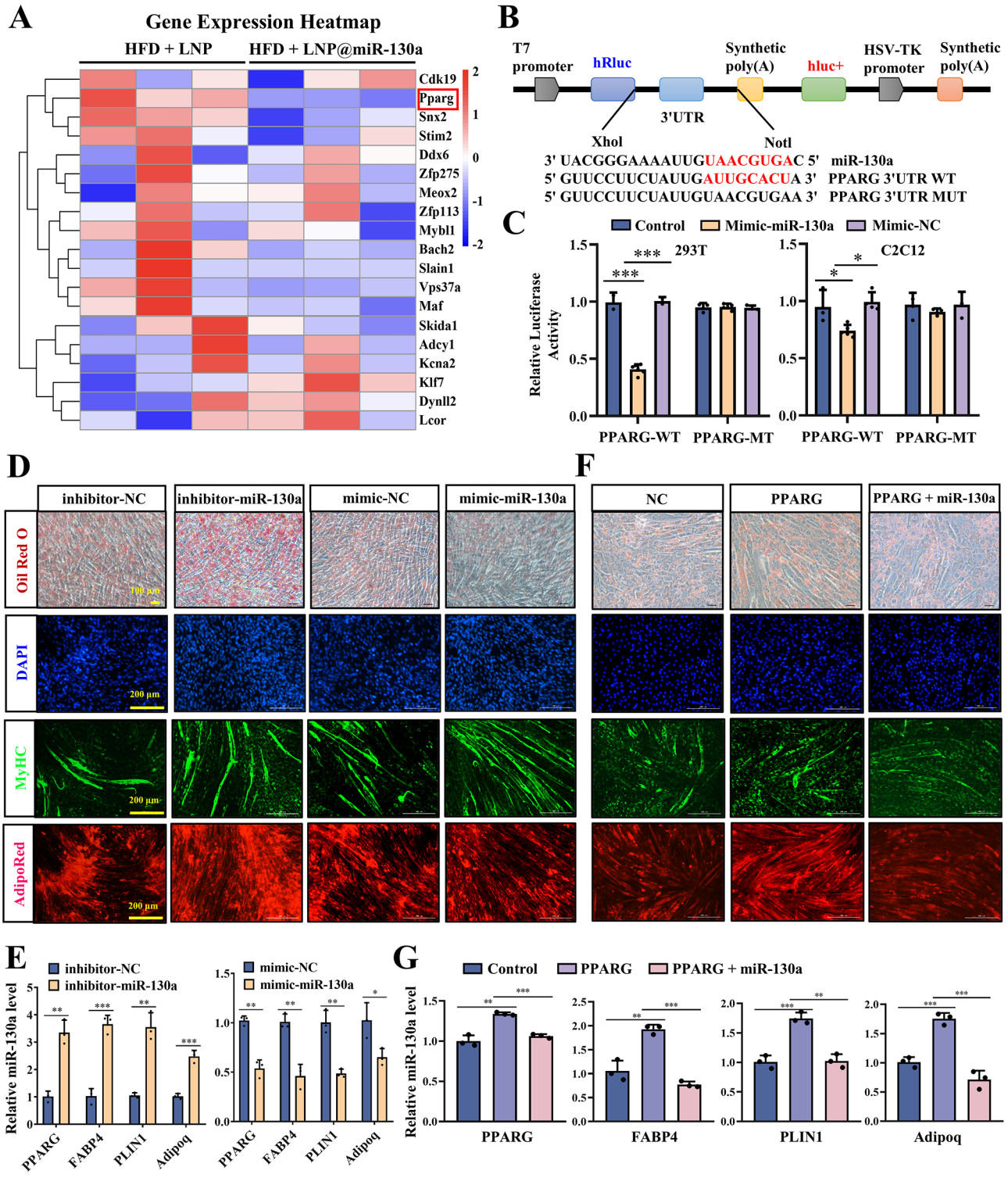

Fig. 5 miR-130a inhibits lipid deposition by targeting PPARG in myoblasts. (**A**) Heatmap of the top 20 target genes of miR-130a in sequencing. (**B**) Pattern diagram of double fluorescent reporter vector. (**C**) Experiment of double fluorescent reporter in 293T cells and C2C12 cells. (**D**) Experiment of Oil Red O and immunofluorescence staining in C2C12 cells treated with miR-130a inhibitor and mimic. (**E**) qPCR of adipogenic genes after add miR-130a's inhibitor and mimic. (**F**) Oil Red O, immunofluorescence staining of C2C12 treated with PPARG and miR-130a. (**G**) qPCR of adipogenic genes of C2C12 treated with PPARG and miR-130a. Scale bars = 200 μm. $^{*}P < 0.05$, $^{**}P < 0.01$, $^{***}P < 0.001$. For each group, $n = 3 \sim 5$. All data are presented as the mean ± SD

S3A shows the successful construction of an adipogenic system in myocytes. After the treatment (Fig S3B), overexpression and inhibition of miR-130a were observed in C2C12 cells (Fig S3C). Staining results showed that miR-130a inhibited adipogenesis in myocytes, significantly reducing lipid droplets and TG content induced by adipogenesis (Fig. 5D, Fig S3D, E, F), and decreasing mRNA expression of adipogenic genes (Fig. 5E). In the recovery experiment, the addition of PPARG counteracted the inhibitory effect of miR-130a on adipogenesis (Fig. 5F, Fig S3G, H), with the mRNA levels of key adipogenic genes was also restored (Fig. 5G).

LNP@miR-130a inhibits obesity in HFD mice by affecting secreting myokines

Interestingly, HFD mice treated with LNP@miR-130a showed a reduction in obesity, while miR-130a is only overexpressed in skeletal muscle. Previous studies suggest that, regulating skeletal muscle homeostasis can counteract weight gain caused by HFD [29, 30], with myokines serves as key messengers in the communication between skeletal muscle regulates adipose tissue and liver [31–33]. To explore the specific mechanisms of muscle-fat and muscle-liver interaction, we analyzed differentially expressed myokines form the transcriptome data. The sequencing results (Fig. 6A) revealed significant changes in many myokines within skeletal muscle. We selected four myokines with significant changes, Metrnl, irisin, IL15, and musclin, and detected them in muscle, serum, brown adipose tissue (BAT), white adipose tissue (WAT) and liver (Fig. 6B). The changes in myokines expression in skeletal muscle were consistent with the sequencing results, and similar changes were observed in serum, WAT, BAT, and liver. Taken together, these findings suggest that the altered level of these myokines in skeletal muscle may be one of the reasons for the changes in serum, and further may affect the expression of myokines in liver and adipose tissue, suggesting a correlation with benign changes in liver and adipose tissue.

LNP@miR-130a relieves obesity in HFD mice

We found that compared to the HFD control groups, the mice treated with LNP@miR-130a exhibited a significant reduction in body temperature (Fig. 6C, Fig. S4A), additionally decreased adipose tissue and with a noticeable change in liver color significantly (Fig. 6C). MRI results show there is a significant decrease in both body fat volume and liver fat percentage (Fig. 6C, Fig. S4B). Liver TG levels decreased following treatment, indicating an improved in fatty liver symptoms in HFD mice (Fig. S4C). Organizational weight analysis also revealed a decrease in visceral WAT, inguinal WAT, BAT, and liver weight (Fig. S4). Furthermore, histological analysis showed that the size of adipocytes in both epididymal and inguinal WAT significantly decreased compared to the control group. Lipid droplets in BAT and liver also decreased significantly, while there were no changes in the group injected with miRNA and LNP alone (Fig. 6C). Serum biochemical indicators of mice (Fig. 7A) revealed the levels of serum TG and cholesterol (CHO) significantly decrease, along with decreased low-density lipoprotein and increased high-density lipoprotein, which is one of the manifestations for weight loss. In addition, liver function biomarkers such as ALT, AST, ALP, and APOB, which showed a trend towards normal levels post-treatment. In order to understand the glucose metabolism function, we conducted intraperitoneal GTT, ITT, and PTT tests. The results showed that after administration, the sensitivity of mice to glucose increased (Fig. 7B, C), and the sensitivity to insulin increased (Fig. 7D, E). HOMA-IR results showed that the degree of insulin resistance in mice decreased and tended towards a healthy level (Fig. 7F), while the metabolic capacity of pyruvate increased (Fig. 7G, H). It is worth noting that there was no significant difference between group CD and group CD + miR-130a, which may be due to the lack of substrate provided by HFD, which prevented the weight loss effect of miR-130a.

In summary, LNP@miR-130a specifically targets skeletal muscle, delivering miR-130a into skeletal muscle cells. MiR-130a directly binds to PPARG, reducing its expression level and inhibiting lipid droplet formation, thereby improving the intracellular environment of myocytes. We found significant changes of four myokines in skeletal muscle, which are consistent with WAT, BAT and liver. Therefore, we speculate that changes in myokines may be one of the reasons for these tissue changes, ultimately leading to weight loss in HFD mice.

Discussion

The development of drugs targeting skeletal muscle has always been a concern for scientists. A recent report, described the use of LNP encapsulation to deliver CRISPR-Cas9 mRNA to skeletal muscle for the treatment of Duchenne muscular dystrophy. They developed a pH dependent ionizable lipid with three hydrophobic tails and formulated it into an LNP delivery system designed to preferentially target skeletal muscle [34]. Their administration method involved repeated intramuscular injections. Additionally, recent reports, researchers used LNP to deliver DNA to cardiomyocytes for the treatment of cardiovascular disease. LNP formulated with a higher DOPE and lower cholesterol molar ratio was used to enhance delivery and GFP expression in cardiomyocytes [35]. And scientists developed a skeletal muscle specific modRNA translation system for LNP encapsulated modRNA, which performs controlled protein translation at the injection site to prevent potential harmful leakage

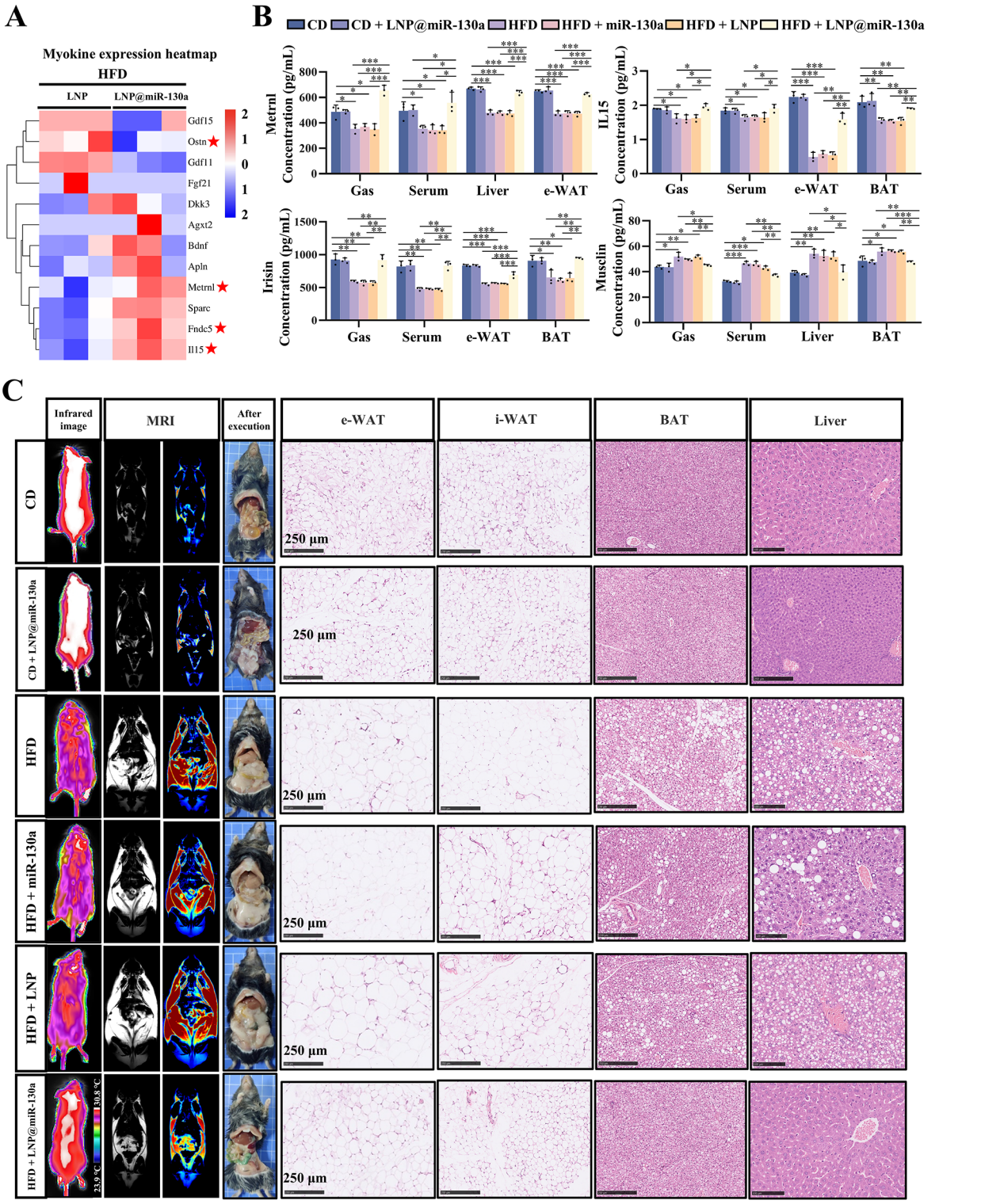

Fig. 6 LNP@miR-130a inhibits obesity by secreting myokines in mice. (**A**) Heatmap of myokines screened in sequencing. (**B**) Myokines content in skeletal muscle (Gas), serum, white fat, brown fat, and liver. $N = 3$. $^{*}P < 0.05$, $^{**}P < 0.01$, $^{***}P < 0.001$. All data are presented as the mean ± SD. (**C**) Infrared images, MRI, photos of mice after execution of 20 w mice and H&E staining of e-WAT, i-WAT, BAT and liver. Scale bars = 250 μm

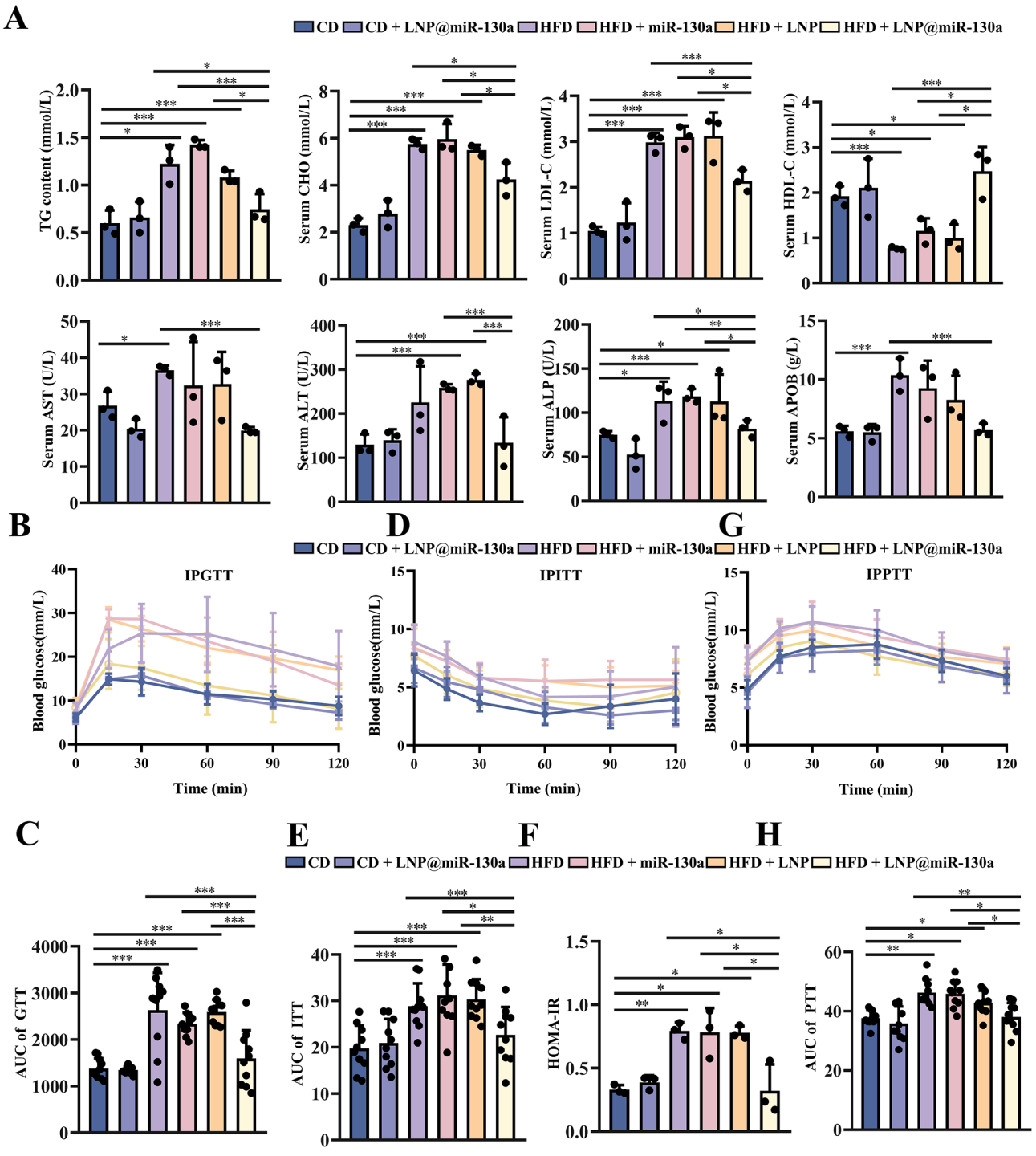

Fig. 7 LNP@miR-130a improves biochemical indicator of blood serum and glucose metabolism in HFD mice. (**A**) Biochemical indicator of blood serum. For each group, $n = 3$. (**B**, **C**) Glucose tolerance testing and area under the curve. (**D**, **E**) Insulin tolerance testing and area under the curve. (**F**) Homeostasis Model Assessment of Insulin Resistance. (**G**, **H**) Acetoacetate tolerance testing and area under the curve. $^{*}P < 0.05$, $^{**}P < 0.01$, $^{***}P < 0.001$. For each group, $n = 10$. All data are presented as the mean ± SD

and expression in non-myocardial and skeletal muscles [36]. At present, there are few studies on products that assemble multiple specific receptors complements onto LNP to improve targeting efficiency.

In this study, we selected five skeletal muscle specific proteins as target molecules. LRP-3 is a transmembrane protein expressed in skeletal muscle and ovaries [37]. As we used male mice as experimental models, off-target

effects from the ovaries could be ruled out. The Myh4 gene encodes MYHC-2B and the Myh2 gene encodes MYHC-2 A, which is involved in muscle fiber formation [38] and is abundantly expressed on the surface of myocytes. MYF5 and MYOG are myogenic regulatory factors (MRFs) involved in regulating skeletal muscle development and regeneration [39], and they are present in the cytoplasm and membrane of muscle cells. Given the abundant expression levels of these five receptors on muscle cell membrane, we designed modified anti-receptors specific to each. Our study is the first to encapsulate these five modified skeletal muscle specific anti-receptors on the surface of artificial LNP, achieving an encapsulation efficiency of up to 99% for miR-130a. It has strong targeting properties for skeletal muscle without off-target effects in the liver, kidney, lung, and pancreas. After 6 weeks of drug administration, the miR-130a carried by LNP still maintained over twice the overexpression efficiency in skeletal muscle, indicating LNP stable retention of LNP in skeletal muscle. This LNP not only delivers miR-130a for the treatment of skeletal muscle lipid deposition abnormalities, but also has the potential to transport nucleic acid drugs for other conditions such as muscle inflammation, muscle atrophy, and muscular dystrophy in the future, with significant application value.

The peroxisome proliferator activated receptor (PPAR) plays a crucial role in regulating energy demand during physical activity. Three subtypes of PPAR have been identified in mammals, with PPARdelta being the predominant subtype in skeletal muscle [40]. PPARG is the primary regulatory factor for adipose tissue generation [41, 42]. Although there is no evidence to suggesting that PPARG is a key gene in skeletal muscle that leads to lipid accumulation, recent studies have found that the absence of PPARG completely eliminates ectopic muscle lipid deposition during muscle regeneration [43]. Additionally, research indicates that the expression of PPARG and C/EBPa is upregulated in elderly individuals with sarcopenia [44, 45], a condition characterized by skeletal muscle fat infiltration [45]. In this study, we observed high expression of PPARG in both the cell model inducing lipid deposition and in a mouse obesity model. LNP@miR-130a regulated the expression of PPARG, resulting in a reduction of TG content in skeletal muscle. A common consequence of obesity is the ectopic storage of fatty acid as TG in skeletal muscle lipid droplets (LDs). In addition, our medication also associated with an increase in the cross-sectional area of muscle fibers, improving muscle mass, and enhancement of athletic performance. In conclusion, we found that PPARG is an important gene regulating lipid deposition in skeletal muscle, and miR-130a acts as an inhibitor of PPARG, which has never been previously confirmed in skeletal muscle in. Thus, PPARG as a promising therapeutic target for addressing lipid deposition abnormalities in skeletal muscle. However, the effects of PPARG and its agonists and inhibitors on skeletal muscle metabolism are still poorly understood [46]. In a study about diabetic sarcopenia, PPARγ inhibition promoted muscle fiber atrophy [47]. Macrophage PPARγ controls GDF3 and skeletal muscle regeneration [48]. Another recent study suggests that, PPARγ/LXRβ pathway activation impede skeletal muscle development and induce lipid accumulation in vivo and in vitro in mice [49]. More studies have shown that PPARG has a protective effect on skeletal muscle insulin resistance [50, 51]. Therefore, the favorable changes in exercise ability and insulin resistance observed in HFD mice after LNP@miR-130a injection in this research may not be entirely dependent on the inhibition of PPARG. On the one hand, the role of PPARG in skeletal muscle growth needs further investigation, and on the other hand, a more detailed mechanism of miR-130a will guide our next research direction.

Researching drugs that directly target skeletal muscles to enhance energy metabolism offers a promising approach to combat obesity, in addition to weight loss surgery, exercise, and dietary control. Obesity is a common disease and a major cause of incidence rate and mortality [52]. Remarkably our developed drug not only targets skeletal muscle accurately, but also reduces body weight, fat mass, insulin sensitivity, and fatty liver levels in mice, effectively inhibiting obesity in HFD mice. Importantly, this effect is not attributed to off-target actions, as miR-130a was not overexpressed in adipose tissue and liver. The interplay between skeletal muscle adipose tissue interaction and skeletal muscle liver interaction is an area of active research. Skeletal muscles play a crucial role in regulating systemic metabolism, partly through the secretion of endocrine factors, collectively known as myokines [53]. In this study, transcriptome sequencing results showed that changes in the RNA expression levels of multiple myokines in mouse skeletal muscle after administration. We speculate that skeletal muscle communicates with adipose tissue and liver by altering myokines levels in the blood. Meteorin-like, also known as Metrnl, plays a crucial role in metabolic regulation [54]. In type 1 and type 2 diabetes mice, the expression of Metrnl in plasma was significantly reduced, and has been shown to mitigate diabetes related cardiomyopathy [55]. Serum Metrnl levels are lower in obese individuals and those with type 2 diabetes compared to healthy controls [56]. Under the HFD, the loss of Metrnl is associated with increased blood TG levels, suggesting its role in lipid regulation [57]. The high level of circulating Metrnl correlate significantly reduced risk of type 2 diabetes [58]. This study also found that the content of Metrnl in muscle has a synergistic relationship with the content of TG in blood, with changes in adipose tissue

and liver those in muscle. Musclin is a myokine that can inhibit palmitate induced endoplasmic reticulum stress by upregulating SIRT7 and autophagy signaling, thereby reducing lipid accumulation in primary liver cells and providing a therapeutic strategy for non-alcoholic fatty liver disease [59]. In obese human subjects and mice, the expression of Musclin in skeletal muscle is significantly increased, resulting in elevated levels of circulating Musclin [60]. In this study, we observed that muscle and serum levels of musclin were elevated in HFD mice, consistent with previous research, and these levels normalized after administration. Interleukin-15 (IL15) which is expressed in skeletal muscle, may serve as a source of plasma IL15 thus regulating adipose tissue [61]. Our findings demonstrate that IL15 increase while PPARG decrease in HFD mice after treatment, contributing to reductions in body weight and fat mass, alleviation of fatty liver, improving glucose homeostasis and insulin sensitivity [62, 63]. Irisin, known for its role in inducing the browning of white adipose tissue, shows a negative correlation with irisin and insulin sensitivity, which aligns with our results [64]. The changes in Metrnl, Musclin, IL15, and Irisin explain the reasons for the alterations in adipose tissue and liver caused by skeletal muscle specific administration.

This study also has limitations. Firstly, PPARG is only one of the target genes of miR-130a, and it cannot be determined that all favorable changes in mice come from the decrease of PPARG. Secondly, the cause of changes in myokines levels in the body cannot be determined yet. Finally, due to the use of LRP3, LNP@miR-130a is only suitable for male mice, and drugs targeting the skeletal muscles of female mice need further research.

In summary, this study demonstrated that LNP @ miR-130a specifically targets skeletal muscle, effectively delivering miR-130a into myocytes and reducing lipid deposition. As skeletal muscle health improves, the changes myokines contribute to alleviating obesity in HFD mice. However, further research is needed to elucidate the specific mechanisms by which skeletal muscle regulate adipose tissue and liver function.

Conclusion

In conclusion, this study successfully developed a targeted lipid nanoparticle carrier with high delivery efficiency and minimal off-target specifically designed for skeletal muscle. This carrier can transport miRNA and other therapeutic molecules, and has strong potential for clinical applications in addressing skeletal muscle lipid deposition abnormalities. Moreover, in the future, this carrier can also be utilized to deliver other small molecule drugs for the treatment of various skeletal muscle diseases. Our findings indicate that LNP carrying miR-130a can significantly improve skeletal muscle lipid deposition, reduce body weight, decrease fat mass, enhance insulin sensitivity, and lower levels of fatty liver in obese mice, providing a novel and effective therapeutic drug strategy for combating obesity.

Materials and methods

Synthesis and characterization of skeletal muscle specific LNP@miR-130a

Ginger nanoparticles were isolated and purified as described in reference [5], and then phospholipid suspensions were prepared using an ULtrasonic Cell Disruptor (with a sound power of 500 W and frequency of 30 kHz) for 15 min at room temperature (25 °C).

LNP formulations were prepared using a procedure similar to a method previously described for mRNA [65, 66]. Briefly, we dissolved three lipids (digalactosyldiacylglycerol, monogalactosyldiacylglycerol, and phosphatidic acid) with dichloromethane (DCM) in glass tubes and mixed them in a ratio of 3:2:5, which mimics the phospholipid composition mixture. Then, phospholipid composition mixture, LRP3, MYF5, MYOG, MYHC-2 A, and MYHC-2B were dissolved in ethanol at molar ratios of 10:1:1:1:1. The lipid mixture was combined with 20 mM citrate buffer (pH 4.0) containing miR-130a at a ratio of 1:12 (ethanol/aqueous) using a microfluidic mixer. Formulations were diluted with 10 times the volume of PBS and dialyzed in dialysis cassettes for at least 24 h, and the mixture was then concentrated using Amicon ULtra centrifugal filters. The LNP formulations were stored at 4 °C.

The nanoparticle morphology was determined by using transmission electron microscopy (TEM; Hitachi H-7500, Japan). The size distribution and concentration of LNPs were examined by nanoparticle tracking analysis with ZetaView PMX 110 (Particle Metrix, Germany) and the corresponding software ZetaView 8.04.02. LNPs were diluted in PBS to measure the particle size and concentration. NTA measurements were recorded and analyzed at 11 positions. Calibration of the ZetaView system was performed using 110 nm polystyrene particles. All procedures were performed at room temperature. According to previous research [67], an agarose gel electrophoresis assay was carried out to evaluate the miRNA loading capacity of LNP.

Animal and sample collection

To establish a high-fat model, 60 male C57BL/6J mice (7 weeks old, purchased from the Experimental Animal Center of Xi'an Jiao-Tong University) were acclimated to the environment for one week and divided into five groups. 20 mice were fed a regular diet (Control Diet, CD, 10% fat) as the control group. The remaining mice were fed a high-fat diet (High-Fat Diet, HFD, 60% fat) to induce obesity. After 14 weeks, the high-fat model was successfully established, and drug administration

commenced. In the CD group, 10 mice were untreated, 10 mice were treated with LNP@miR-130a. In the HFD group, 10 mice were left untreated, 10 mice were treated with naked miR-130a only (provided by Hanheng, China), 10 were treated with Lipid Nanoparticles (LNP) only, and 10 were treated with LNP encapsulated miR-130a (LNP@miR-130a). Mice were treated with LNP at a dosage of 10 mg/kg body weight. The control group was treated with 0.9% NaCl. Injections were administered seven times over a period of three weeks. Live experiments began at 17 weeks, and mice were euthanized at 20 weeks. Skeletal muscle, white adipose tissue, brown adipose tissue, liver, and serum were collected for further analysis. The animal experiments were approved by the Research Ethics Committee of Northwest A&F University (approval number 2011-31101684).

Chemical imaging

To elucidate the biodistribution of lipid nanoparticles encapsulating miR-130a (LNPs@miR-130a), the IVIS Lumina Imaging System (Caliper Life Sciences, Hopkinton, MA, USA) was employed for in vivo fluorescence imaging [68]. LNPs@miR-130a coupled with the near-infrared fluorescent dye Cy7 enables visualization and tracking of nanoparticles in mice to achieve deep tissue penetration and minimal background autofluorescence.

Thermal imaging analysis

Mouse subjects were evaluated thermographically using a high-resolution infrared imaging device, FLIR ONE PRO Thermal Camera (FLIR Systems, Wilsonville, OR, USA) [69]. Subsequently, the captured thermograms were analyzed in detail using FLIR software to process and enhance the infrared images, allowing accurate temperature measurements and detection of thermal patte.

Glucose tolerance test (GTT), insulin tolerance test (ITT), and pyruvate tolerance test (PTT)

Prior to the commencement of metabolic assays, mice were subjected to fasting to standardize the experimental conditions. Specifically, for the GTT and PTT, a 16-hour fasting period was implemented, whereas for the ITT, a 4-hour fasting period was observed.

After the fasting period, each mouse was weighed to obtain its baseline weight. A small section of the mouse's tail was excised and gently pressed to induce blood flow, and then blood samples were collected for analysis.

Fasting blood glucose levels were determined using a calibrated blood glucose meter (YUWELL, Jiangsu, China), which provides a rapid and accurate measurement of glucose concentrations in the blood samples. Following the baseline glucose measurement, a glucose solution (1.5 g/kg body weight), insulin (0.65 U/kg body weight), or sodium pyruvate (1.5 g/kg body weight) was administered via intraperitoneal injection.

After injection, blood glucose levels were monitored at specific time intervals (15, 30, 60, 90, and 120 min) to capture the dynamic response of glucose metabolism in mice after injection of the challenge substance to assess changes in glucose homeostasis and insulin sensitivity [70].

Running test, swimming test, and suspension test

To evaluate the physical endurance and exercise capacity of mice, each having undergone an 18-week treatment regimen, were subjected to a series of standardized physical performance tests. The protocols refer to the following references and be modified according to the actual situation [71–73].

Treadmill fatigue test

The treadmill fatigue test was employed to quantify the endurance capacity of the mice. Before the commencement of the test, the subjects underwent a three-day acclimatization period on an electrified treadmill, during which they were required to run at a uniform velocity of 10 m per minute for a duration of 30 min. The actual fatigue test initiated at the same speed of 10 m/min, with the velocity incrementally increased by 1 m/min at each minute interval. The endpoint of exhaustion was defined as the inability of the mouse to continue running after a 5-second period of continuous electrical stimulation (1 Hz, 0.15 mA, 163 V) delivered to the treadmill grid.

Swimming test

The swimming capacity of the mice was assessed using acrylic resin cylinders with a diameter of 19 cm and a height of 50 cm, filled with tap water maintained at a temperature of 23–24 °C, with a water depth of 20 cm. Each mouse was subjected to a load equivalent to 10% of its body weight to simulate a natural swimming condition. The test measured the duration for which the mouse was able to keep its mouth and nose above water continuously, which is an indicator of the mouse's swimming stamina and physical endurance. The swimming time was recorded from the moment the mouse was placed in the water until it failed to keep its head above water for a continuous period of 3 s, at which point the test was terminated to prevent drowning.

Suspension test

In the suspension test, mice were inverted and suspended from a 20 cm × 20 cm metal mesh, with each small grid measuring 0.5 cm^2. The test recorded the duration for which the mice were able to maintain their grip before succumbing to gravity and dropping from the mesh. This

test provides a measure of the mice's muscular strength and endurance under conditions of physical stress.

Magnetic resonance imaging (MRI)

Anesthesia was induced in the mice using isoflurane to ensure their comfort and immobility during imaging. The mice were positioned horizontally within the MRI scanner to allow for a comprehensive body scan.

Anesthesia was induced in the mice using isoflurane to ensure their comfort and immobility during imaging. The mice were positioned horizontally within the MRI scanner to allow for a comprehensive body scan. Anesthesia was induced in the mice using isoflurane to ensure their comfort and immobility during imaging. The mice were positioned horizontally within the MRI scanner to allow for a comprehensive body scan.

The MRI protocol involved the acquisition of 18 distinct slices covering the entire body. The body composition, including liver and body fat, was assessed using this high-field strength MRI. Lipid quantification was performed by analyzing the signals from the liver fat or body fat, with representative images selected from the middle section that covered 8 slices [74]. The fourth slice from this middle section was specifically used for the analysis.

Hematoxylin and Eosin (H&E) staining

Fix muscle tissue with 4% paraformaldehyde for paraffin and frozen sections. After dewaxing, the paraffin sections were stained with hematoxylin and eosin and observed under a microscope.

Manually circle the cross-sectional shape of muscle fibers and use Image J software (NIH) to calculate the cross-sectional area measurement. Each muscle uses at least 500 fibers to calculate its cross-sectional area [79].

Fluorescence staining

The treated cells were discarded from the culture medium, washed with PBS for 2 times, added appropriate amount of fixative, and fixed at room temperature for 30 min. Discarded the fixative, washed with PBS for 2 times, added appropriate amount of 0.5% Triton X-100, and permeabilized at room temperature for 30 min. Washed with PBS for 2 times, and closed at room temperature for 30 min with 5% BSA. Diluted the primary antibody according to the appropriate proportion, and left at 4℃ overnight. Washed with PBS for 2 times, and diluted the secondary antibody according to the appropriate proportion, and photographed after 1 h at room temperature. Dilute the secondary antibody according to the appropriate proportion, and take pictures after 1 h at room temperature [75]. The same experimental protocol was used for mice tissue section.

Succinate dehydrogenase (SDH) staining

The experimental protocol is based on the instructions of the reagent kit (Solarbio, G2000, China). Take fresh tissue that cannot be fixed, prepare frozen slices, add NBT incubation solution dropwise to the slices, and place them in a 37 ℃ incubator for 5–30 min of constant temperature staining. Gently rinse with distilled water to remove excess dye. Observe and take photos under a microscope.

Myokines detection

Add 50ul of diluted standard and 50ul of test sample to each reaction well. Immediately add 50ul of biotin-labeled antibody. Cover the plate and mix gently, incubate at 37℃ for 1 h. Discard the liquid and wash 3 times with washing solution. Add 80ul of streptavidin-HRP to each well, mix gently, and incubate at 37℃ for 30 min. Discard the liquid and wash 3 times with washing solution. Add 50ul of the corresponding substrate to each well, mix gently, and incubate at 37℃ for 10 min, avoiding light. Remove the microplate and quickly add 50ul of stop solution. After adding the stop solution, measure the results immediately [76]. Measure the OD value of each well at the specified wavelength.

Serum biochemical profiling

Following the experimental protocol, blood samples were collected from the subjects at the conclusion of the study [77]. The samples were centrifuged at 3000 rpm for 10 min at 4 °C to isolate the serum. The biochemical analysis was performed at the Biochemical Analysis Laboratory within the School of Animal Science and Technology at Northwest A&F University, Yangling, Shaanxi, China. A range of biochemical parameters were measured, including glucose, lipids, liver function markers, and electrolytes, using validated analytical techniques and high-precision instruments to assess the metabolic status of the subjects.

Measurement of triglyceride (TG) levels in muscle tissue

To quantify triglyceride (TG) content within muscle tissue, a TG assay kit from Solabio (Beijing, China) was employed. The absorbance was measured at 450 nm using an ELISA spectrophotometer (model 51119080, Thermo Fisher, Waltham, USA), which was calibrated prior to use to ensure accurate readings [78]. TG levels were determined by comparing the absorbance values to a standard curve generated from the kit's TG standards.

Cell culture and transfection

C2C12 cells (ATCC) were cultured in high-glucose DMEM (Gibco) supplemented with 10% FBS and 1% penicillin/streptomycin at 37 °C and 5% CO2. Cells were seeded into 6, 12, and 24-well plates and transfected with miR-130a mimics or inhibitors (Ribobio) at a

concentration of 50 nmol/L, using X-tremeGene siRNA transfection reagent (Roche) and Opti-MEM medium (Gibco). After 12 h, the medium was replaced with fresh culture medium.

To induce cell differentiation, DMEM containing 2% horse serum (Gibco) was used [79]. After 7 d of myotube formation, cells were incubated with DMEM containing 0.5% fatty acid-free BSA and 500 μm oleic acid ester (Aladdin) for 24 h before harvesting.

Total RNA extraction, RNA Reverse Transcription, and RT qPCR

Tissue or cell lysate was transferred to a 1.5mL RNase-free EP tube, add an appropriate amount of TRIzol, and let it stand for 5 min. Add 200μL of chloroform to each tube, mixed thoroughly, and incubated on ice for 10 min and the samples were centrifuged at 4 °C for 15 min. After centrifugation, transferred the upper aqueous phase (approximately 500μL) to a new EP tube. The sample was incubated on ice and precipitated with alcohol for 10 min. Centrifuge and remove the supernatant and wash the RNA pellet with 1mL of 75% ethanol. The supernatant was removed, and the RNA pellet was air-dried or vacuum-dried for 5–10 min and then resuspended with appropriate amount of water.

The extracted RNA was reverse transcribed using a two-step method. Quantitative RT-PCR was performed using qPCR SYBR Green Premix on a real-time PCR system. The expression of the target gene was normalized to the average expression of the control group [80].

Luciferase reporter gene assay methodology

The plasmid pis-CHECK2, which includes the wild-type and mutant 3'-untranslated regions (3'-UTRs) of the PPARG gene, was sourced from General Biosystems Co., Ltd. (Anhui, China). HEK293T and C2C12 cells were seeded in 48-well plates and co-transfected with the 3'-UTR constructs and miR-130a mimic using Lipofectamine 2000. Luciferase activity was assessed in cell lysates utilizing the Dual Glo Luciferase Assay System from Promega (Madison, WI) [81].

Statistical analysis

Statistical analysis was performed using two-way ANOVA and multiple t-test in GraphPad Prism version 8 statistical software (La Jolla). The data presented as ± SEM mean, with $P < 0.05$ is considered significant * $P < 0.05$, ** $P < 0.01$, *** $P < 0.001$.

Supplementary Information

The online version contains supplementary material available at https://doi.org/10.1186/s12951-025-03225-0.

Supplementary Material 1: Figure S1 LNP@miR-130a increases lipid deposition of Qu and TA in HFD mice

Supplementary Material 2: Figure S2 LNP@miR-130a increases number of type I muscle fibers

Supplementary Material 3: Figure S3 miR-130a inhibits lipid deposition and overexpression of PPARG offset this inhibition

Supplementary Material 4: Figure S4 LNP@miR-130a affects WAT, liver, BAT of the HFD mice

Supplementary Material 5: Table S1 The primer sequences and parameters used for real-time qPCR

Acknowledgements

We thank Dr. Weike Shaoyong and Dr. Lili Sun from Shanghai Jiao Tong University for their expert assistance with echo experimental design and excellent technical assistance.

Author contributions

Yingqian Wang, Zeqiang Ma and Lehua Jiang designed, performed experiments and drafted the manuscript. Nataraj Bojan, Yiwen Sha, Boyu Huang, Junnan Shen analyzed the results of the experiments. Nataraj Bojan polished the language. Weijun Pang provided funding support and revised the manuscript. All authors approved the final version of this manuscript. All authors read and approved the final manuscript.

Funding

This work was supported by grants from the National Natural Science Foundations of China (32272847, 31572366 and U22A20516), the earmarked fund for CARS-35-PIG, and the Key Research and Development Program of Shaanxi Province (2022ZDLNY01-04).

Data availability

No datasets were generated or analysed during the current study.

Declarations

Ethics approval and consent to participate

All animal experiments complied with current ethical considerations and were conducted with the formal approval of the Ethical Committee (Northwest A&F University, China).

Consent for publication

Not applicable.

Competing interests

The authors declare no competing interests.

Author details

[1]Laboratory of Animal Fat Deposition and Muscle Development, College of Animal Science and Technology, Northwest A&F University, Shaanxi, China
[2]Center for Metabolic & Gastroenterology, Institute of Translational Medicine, Shanghai Jiao Tong University School of Medicine, Shanghai, China
[3]Department of Toxicology and Sanitary Chemistry, School of Public Health, Tianjin Medical University, Tianjin, China
[4]College of Animal Science and Technology, Anhui Agricultural University, Hefei, China
[5]No. 22 Xinong Road, Yangling, Shaanxi Province 712100, China

Received: 30 September 2024 / Accepted: 11 February 2025
Published online: 03 March 2025

References

1. Cullis PR, Felgner PL. The 60-year evolution of lipid nanoparticles for nucleic acid delivery. Nat Rev Drug Discov. 2024;23:709–22.

2. Akinc A, Maier MA, Manoharan M, Fitzgerald K, Jayaraman M, Barros S, et al. The Onpattro story and the clinical translation of nanomedicines containing nucleic acid-based drugs. Nat Nanotechnol. 2019;14:1084–87.
3. Sáez-Llorens X, Lanata C, Aranguren E, Celis CR, Cornejo R, DeAntonio R, et al. Safety and immunogenicity of mRNA-LNP COVID-19 vaccine CVnCoV in latin American adults: a phase 2 randomized study. Vaccine: X. 2022;11:100189.
4. Tenchov R, Bird R, Curtze AE, Zhou Q. Lipid NanoparticlesFrom liposomes to mRNA vaccine delivery, a Landscape of Research Diversity and Advancement. ACS Nano. 2021;15(11):16982–7015.
5. Kumar A, Sundaram K, Teng Y, Mu J, Sriwastva MK, Zhang L, et al. Ginger nanoparticles mediated induction of Foxa2 prevents high-fat diet-induced insulin resistance. Theranostics. 2022;12:1388–403.
6. Yan L, Cao Y, Hou L, Luo T, Li M, Gao S et al. Ginger exosome-like nanoparticle-derived miRNA therapeutics: a strategic inhibitor of intestinal inflammation. J Adv Res. 2024;24:130–9.
7. Ebner DC, Bialek P, El-Kattan AF, Ambler CM, Tu M. Strategies for skeletal muscle targeting in drug discovery. Curr Pharm Des. 2015;21:1327–36.
8. Saber N, Senti ME, Schiffelers RM. Lipid nanoparticles for nucleic acid delivery beyond the liver. Hum Gene Ther. 2024;35:617–27.
9. He X, Chang Z, Chen F, Zhang W, Sun M, Shi T, et al. Engineering a biomimetic system for hepatocyte-specific RNAi treatment of non-alcoholic fatty liver disease. Acta Biomater. 2024;174:281–96.
10. Rizvi F, Lee YR, Diaz-Aragon R, Bawa PS, So J, Florentino RM, et al. VEGFA mRNA-LNP promotes biliary epithelial cell-to-hepatocyte conversion in acute and chronic liver diseases and reverses steatosis and fibrosis. Cell Stem Cell. 2023;30:1640–57.
11. Yang T, Poenisch M, Khanal R, Hu Q, Dai Z, Li R, et al. Therapeutic HNF4A mRNA attenuates liver fibrosis in a preclinical model. J Hepatol. 2021;75:1420–33.
12. Du X, Yada E, Terai Y, Takahashi T, Nakanishi H, Tanaka H et al. Comprehensive evaluation of lipid nanoparticles and polyplex nanomicelles for muscle-targeted mRNA delivery. Pharm 2023;15.
13. Henin G, Loumaye A, Leclercq IA, Lanthier N. Myosteatosis: diagnosis, pathophysiology and consequences in metabolic dysfunction-associated steatotic liver disease. JHEP Rep. 2024;6:100963.
14. Zhang W, Yang D, Yuan Y, Liu C, Chen H, Zhang Y, et al. Muscular G9a regulates muscle-liver-Fat Axis by Musclin under Overnutrition in Female mice. Diabetes. 2020;69:2642–54.
15. Samuel VT, Shulman GI. Mechanisms for insulin resistance: common threads and missing links. Cell. 2012;148:852–71.
16. Devarshi PP, McNabney SM, Henagan TM. Skeletal muscle nucleo-mitochondrial crosstalk in obesity and type 2 diabetes. Int J Mol Sci. 2017;18.
17. Gilbert M. Role of skeletal muscle lipids in the pathogenesis of insulin resistance of obesity and type 2 diabetes. J Diabetes Investig. 2021;12:1934–41.
18. Campolo F, Catanzaro G, Venneri MA, Ferretti E, Besharat ZM. MicroRNA loaded edible nanoparticles: an emerging personalized therapeutic approach for the treatment of obesity and metabolic disorders. Theranostics. 2022;12:2631–34.
19. Ying W, Gao H, Dos Reis FCG, Bandyopadhyay G, Ofrecio JM, Luo Z, et al. MiR-690, an exosomal-derived miRNA from M2-polarized macrophages, improves insulin sensitivity in obese mice. Cell Metab. 2021;33:781–90.
20. Liu Y, Yang Y, Xu C, Liu J, Chen J, Li G, et al. Circular RNA circGlis3 protects against islet β-cell dysfunction and apoptosis in obesity. Nat Commun. 2023;14:351.
21. Wang M, Su L, Sun J, Cai L, Li X, Zhu X, et al. FGF21 attenuates pulmonary arterial hypertension via downregulation of miR-130, which targets PPARγ. J Cell Mol Med. 2022;26:1034–49.
22. Yuan Y, Peng W, Liu Y, Xu Z. Circulating miR-130 and its target PPAR-γ may be potential biomarkers in patients of coronary artery disease with type 2 diabetes mellitus. Mol Genet Genomic Med. 2019;7:e909.
23. Kudo T, Zhao ML, Jeknić S, Kovary KM, LaGory EL, Covert MW, et al. Context-dependent regulation of lipid accumulation in adipocytes by a HIF1α-PPARγ feedback network. Cell Syst. 2023;14:1074–86.
24. Väremo L, Henriksen TI, Scheele C, Broholm C, Pedersen M, Uhlén M, et al. Type 2 diabetes and obesity induce similar transcriptional reprogramming in human myocytes. Genome Med. 2017;9:47.
25. Zong Y, Lin Y, Wei T, Cheng Q. Lipid nanoparticle (LNP) enables mRNA delivery for Cancer Therapy. Adv Mater. 2023;35:e2303261.
26. Kiaie SH, Majidi Zolbanin N, Ahmadi A, Bagherifar R, Valizadeh H, Kashanchi F, et al. Recent advances in mRNA-LNP therapeutics: immunological and pharmacological aspects. J Nanobiotechnol. 2022;20:276.
27. Ash GI, Kim D, Choudhury M. Promises of nanotherapeutics in obesity. Trends Endocrinol Metab. 2019;30:369–83.
28. Ji J, Lefebvre E, Laporte J. Comparative in vivo characterization of newly discovered myotropic adeno-associated vectors. Skelet Muscle. 2024;14:9.
29. Guo A, Li K, Tian HC, Fan Z, Chen QN, Yang YF, et al. FGF19 protects skeletal muscle against obesity-induced muscle atrophy, metabolic derangement and abnormal irisin levels via the AMPK/SIRT-1/PGC-α pathway. J Cell Mol Med. 2021;25:3585–600.
30. Shen S, Liao Q, Zhang T, Pan R, Lin L. Myricanol modulates skeletal muscle-adipose tissue crosstalk to alleviate high-fat diet-induced obesity and insulin resistance. Br J Pharmacol. 2019;176:3983–4001.
31. Bilski J, Pierzchalski P, Szczepanik M, Bonior J, Zoladz JA. Multifactorial mechanism of Sarcopenia and Sarcopenic Obesity. Role of Physical Exercise, Microbiota and Myokines. Cells. 2022;11.
32. Park MJ, Choi KM. Interplay of skeletal muscle and adipose tissue: sarcopenic obesity. Metabolism. 2023;144:155577.
33. Polyzos SA, Vachliotis ID, Mantzoros CS. Sarcopenia, sarcopenic obesity and nonalcoholic fatty liver disease. Metabolism. 2023;147:155676.
34. Kenjo E, Hozumi H, Makita Y, Iwabuchi KA, Fujimoto N, Matsumoto S, et al. Low immunogenicity of LNP allows repeated administrations of CRISPR-Cas9 mRNA into skeletal muscle in mice. Nat Commun. 2021;12:7101.
35. Scalzo S, Santos AK, Ferreira HAS, Costa PA, Prazeres P, da Silva NJA, et al. Ionizable lipid nanoparticle-mediated delivery of plasmid DNA in Cardiomyocytes. Int J Nanomed. 2022;17:2865–81.
36. Żak MM, Kaur K, Yoo J, Kurian AA, Adjmi M, Mainkar G et al. Modified mRNA Formulation and Stability for Cardiac and skeletal muscle delivery. Pharmaceutics. 2023;15.
37. Ishii H, Kim DH, Fujita T, Endo Y, Saeki S, Yamamoto TT. cDNA cloning of a new low-density lipoprotein receptor-related protein and mapping of its gene (LRP3) to chromosome bands 19q12-q13. 2. Genomics. 1998;51:132–35.
38. Schiaffino S. Muscle fiber type diversity revealed by anti-myosin heavy chain antibodies. FEBS J. 2018;285:3688–94.
39. Vicente-García C, Hernández-Camacho JD, Carvajal JJ. Regulation of myogenic gene expression. Exp Cell Res. 2022;419:113299.
40. Mengeste AM, Rustan AC, Lund J. Skeletal muscle energy metabolism in obesity. Obes (Silver Spring). 2021;29(10):1582–95.
41. Foley B, Doheny DL, Black MB, Pendse SN, Wetmore BA, Clewell RA, et al. editors. 's Highlight: Screening ToxCast Prioritized Chemicals for PPARG Function in a Human Adipose-Derived Stem Cell Model of Adipogenesis. Toxicol Sci. 2017; 155:85–100.
42. Poissonnet CM, Burdi AR, Bookstein FL. Growth and development of human adipose tissue during early gestation. Early Hum Dev. 1983;8:1–11.
43. Dammone G, Karaz S, Lukjanenko L, Winkler C, Sizzano F, Jacot G et al. PPARγ controls ectopic adipogenesis and cross-talks with myogenesis during skeletal muscle regeneration. Int J Mol Sci. 2018;19.
44. Lee D, Kuroki T, Nagai T, Kawano K, Higa K, Kurogi S et al. Sarcopenia, Ectopic Fat Infiltration Into the Lumbar Paravertebral Muscles, and Lumbo-Pelvic Deformity in Older Adults Undergoing Lumbar Surgery. Spine. 2022; 47:E46–57.
45. Xu Z, You W, Chen W, Zhou Y, Nong Q, Valencak TG, et al. Single-cell RNA sequencing and lipidomics reveal cell and lipid dynamics of fat infiltration in skeletal muscle. J Cachexia Sarcopenia Muscle. 2021;12:109–29.
46. Crossland H, Constantin-Teodosiu D, Greenhaff PL. The Regulatory roles of PPARs in skeletal muscle fuel metabolism and inflammation: impact of PPAR agonism on muscle in Chronic Disease, Contraction and Sepsis. Int J Mol Sci, 2021;22(18).
47. Yan SB, et al. Stimulator of interferon genes promotes diabetic Sarcopenia by targeting peroxisome proliferator activated receptors γ degradation and inhibiting fatty acid oxidation. J Cachexia Sarcopenia Muscle. 2023;14(6):2623–41.
48. Varga T, et al. Macrophage PPARγ, a lipid activated transcription factor controls the growth factor GDF3 and skeletal muscle regeneration. Immunity. 2016;45(5):1038–51.
49. Xu R, et al. Polystyrene nano-plastics impede skeletal muscle development and induce lipid accumulation via the PPARγ/LXRβ pathway in vivo and in vitro in mice. Arch Toxicol. 2024;98(11):3713–25.
50. Amin RH, et al. Selective activation of PPARgamma in skeletal muscle induces endogenous production of adiponectin and protects mice from diet-induced insulin resistance. Am J Physiol Endocrinol Metab. 2010;298(1):E28–37.
51. Hevener AL, et al. Muscle-specific Pparg deletion causes insulin resistance. Nat Med. 2003;9(12):1491–7.

52. Gilden AH, Catenacci VA, Taormina JM, Obesity. Ann Intern Med. 2024;177(5):Itc65–80.
53. Eckardt K, Görgens SW, Raschke S, Eckel J. Myokines in insulin resistance and type 2 diabetes. Diabetologia. 2014;57:1087–99.
54. Rao RR, Long JZ, White JP, Svensson KJ, Lou J, Lokurkar I, et al. Meteorin-like is a hormone that regulates immune-adipose interactions to increase beige fat thermogenesis. Cell. 2014;157:1279–91.
55. Lu QB, Ding Y, Liu Y, Wang ZC, Wu YJ, Niu KM, et al. Metrnl ameliorates diabetic cardiomyopathy via inactivation of cGAS/STING signaling dependent on LKB1/AMPK/ULK1-mediated autophagy. J Adv Res. 2023;51:161–79.
56. Alizadeh H. Meteorin-like protein (Metrnl): a metabolic syndrome biomarker and an exercise mediator. Cytokine. 2022;157:155952.
57. Qi Q, Hu WJ, Zheng SL, Zhang SL, Le YY, Li ZY, et al. Metrnl deficiency decreases blood HDL cholesterol and increases blood triglyceride. Acta Pharmacol Sin. 2020;41:1568–75.
58. Zhou Y, Liu L, Jin B, Wu Y, Xu L, Chang X, et al. Metrnl alleviates lipid Accumulation by modulating mitochondrial homeostasis in Diabetic Nephropathy. Diabetes. 2023;72:611–26.
59. Cho W, Choi SW, Oh H, Baygutalp F, Abd El-Aty AM, Jeong JH, et al. Musclin attenuates lipid deposition in hepatocytes through SIRT7/autophagy-mediated suppression of ER stress. Biochem Biophys Res Commun. 2023;658:62–8.
60. Nielsen AR, Hojman P, Erikstrup C, Fischer CP, Plomgaard P, Mounier R, et al. Association between interleukin-15 and obesity: interleukin-15 as a potential regulator of fat mass. J Clin Endocrinol Metab. 2008;93:4486–93.
61. Sun H, Ma Y, Gao M, Liu D. IL-15/sIL-15Rα gene transfer induces weight loss and improves glucose homeostasis in obese mice. Gene Ther. 2016;23:349–56.
62. Sun H, Liu D. Hydrodynamic delivery of interleukin 15 gene promotes resistance to high fat diet-induced obesity, fatty liver and improves glucose homeostasis. Gene Ther. 2015;22:341–47.
63. Boström P, Wu J, Jedrychowski MP, Korde A, Ye L, Lo JC, et al. A PGC1-α-dependent myokine that drives brown-fat-like development of white fat and thermogenesis. Nature. 2012;481:463–68.
64. Sesti G, Andreozzi F, Fiorentino TV, Mannino GC, Sciacqua A, Marini MA, et al. High circulating irisin levels are associated with insulin resistance and vascular atherosclerosis in a cohort of nondiabetic adult subjects. Acta Diabetol. 2014;51:705–13.
65. Zhang NN, Li XF, Deng YQ, Zhao H, Huang YJ, Yang G, et al. A thermostable mRNA vaccine against COVID-19. Cell. 2020;182:1271–83.
66. Bahl K, Senn JJ, Yuzhakov O, Bulychev A, Brito LA, Hassett KJ, et al. Preclinical and clinical demonstration of immunogenicity by mRNA vaccines against H10N8 and H7N9 influenza viruses. Mol Ther. 2017;25:1316–27.
67. Wang M, Alberti K, Varone A, Pouli D, Georgakoudi I, Xu Q. Enhanced intracellular siRNA delivery using bioreducible lipid-like nanoparticles. Adv Healthc Mater. 2014;3:1398–403.
68. Sevieri M et al. Tumor Accumulation and off-target Biodistribution of an indocyanine-green fluorescent nanotracer: an Ex vivo study on an orthotopic murine model of breast Cancer. Int J Mol Sci, 2021;22(4).
69. Machado AS, et al. Influence of infrared camera model and evaluator reproducibility in the assessment of skin temperature responses to physical exercise. J Therm Biol. 2021;98:102913.
70. Liu J, et al. GDF15 negatively regulates RGS16 to impair hepatic lipid metabolism in male mice offspring conceived by in vitro fertilization. Am J Transl Res. 2022;14(10):7535–51.
71. Bulmus O, et al. Treadmill exercise training improves the high-fat diet-induced behavioral changes in the male rats. Biol Futur. 2022;73(4):483–93.
72. Chen YM, et al. Sake protein supplementation affects Exercise performance and biochemical profiles in Power-Exercise-trained mice. Nutrients. 2016;8(2):106.
73. Janice Sánchez B, et al. Depletion of HuR in murine skeletal muscle enhances exercise endurance and prevents cancer-induced muscle atrophy. Nat Commun. 2019;10(1):4171.
74. Subhani M, et al. Association between glucagon-like peptide-1 receptor agonists use and change in alcohol consumption: a systematic review. EClinicalMedicine. 2024;78:102920.
75. Gan Y, et al. Chitosan-based injectable porous microcarriers with enhanced adipogenic differentiation and angiogenesis for subcutaneous adipose tissue regeneration. Biomater Adv. 2025;169:214174.
76. Us Altay D, et al. Non-alcoholic fatty liver disease: the importance of physical activity and nutrition education-A randomized controlled study. J Gastroenterol Hepatol. 2024;39(12):2723–34.
77. V G, et al. Production performance, serum lipid profile and gut health in Indian native Kadaknath chickens fed diet incorporated with liquorice root powder. Heliyon. 2024;10(22):e40230.
78. Peng Z, et al. 6-Gingerol improves lipid metabolism disorders in skeletal muscle by regulating AdipoR1/AMPK signaling pathway. Biomed Pharmacother. 2024;180:117462.
79. Rojas-Sanchez L, et al. Genetic immunization against hepatitis B virus with calcium phosphate nanoparticles in vitro and in vivo. Acta Biomater. 2020;110:254–65.
80. Zhao L, et al. Effect of plasma exosome lncRNA on isoproterenol hydrochloride-induced cardiotoxicity in rats. Toxicol Appl Pharmacol. 2024;484:116840.
81. Li X, et al. Bioinformatics in vivo and in vitro assays identified mir-486-5p as a tumor suppressor miRNA in hepatocellular carcinoma. Heliyon. 2024;10(24):e39909.

Publisher's note